metals

MDPI

Article

Comparative Analysis of the Hot Isostatic Pressing Densification Behavior of Uniform and Non-Uniform Distributed Powder

Fandi Meng *, Lihui Lang † and Yi Xiao

School of Mechanical Engineering and Automation, Beihang University, Beijing 100191, China
* Correspondence: mengfandi@buaa.edu.cn
† Deceased author.

Abstract: Hot isostatic pressing (HIP) technology can directly produce nearly clean shaped workpieces that meet the requirements while ensuring machining accuracy and surface quality. Usually, people use numerical simulation methods to reduce experimental costs. Generally, a uniform powder relative density distribution of about 65% is used in the simulation. However, in practical engineering, we found that even with additional tools such as vibration tables, the powder filling is not uniform. The non-uniform distribution causes uneven shrinkage of the powder and capsule after HIP. In this paper, a numerical model for HIPing of Ti-6Al-4V powder is developed to improve the prediction by comparing the uniform and non-uniform initial powder distribution. The results show that different initial relative density distributions affect the powder densification process and further affect the deformation of the capsule. It also leads to non-uniform stress distribution after HIP, which increases the risk of capsule rupture. The analysis of the numerical simulation results and the comparison with the experimental results highlights that taking into account the non-uniform powder distribution inside the capsule is vital to improve numerical results and produce near-net shape components. The maximum error of the simulation with the usual initial relative density setting of 65% is 4.2%. However, considering the uneven distribution of initial powder, the maximum error is reduced to 3.16%, and the average error is also less than 2%.

Keywords: hot isostatic pressing (HIP); initial powder distribution; numerical simulation; densification

check for updates

Citation: Meng, F.; Lang, L.; Xiao, Y. Comparative Analysis of the Hot Isostatic Pressing Densification Behavior of Uniform and Non-Uniform Distributed Powder. *Metals* **2023**, *13*, 1319. https://doi.org/10.3390/met13071319

Academic Editors: Mariola Saternus and Ladislav Socha

Received: 8 June 2023
Revised: 3 July 2023
Accepted: 4 July 2023
Published: 24 July 2023

Copyright: © 2023 by the authors. Licensee MDPI, Basel, Switzerland. This article is an open access article distributed under the terms and conditions of the Creative Commons Attribution (CC BY) license (https://creativecommons.org/licenses/by/4.0/).

1. Introduction

Ti6Al4V alloy has been widely used in aviation, aerospace, ships, and other fields due to its characteristics of low density, high specific strength, strong corrosion resistance, and excellent comprehensive properties [1]. To meet the high-performance requirements of aerospace parts, the structures of various parts are becoming increasingly complex. At present, the traditional casting, forging, diffusion bonding, and 3D printing technologies have their defects and difficulties in realizing the forming of complex high-performance structural components [2–5]. As a new near-net shaping method, powder metallurgy combined with hot isostatic pressing (HIP) [6], can form complex parts. The mechanical properties of the formed parts are equivalent to those of the forged alloy. In the process of HIP, the densification process of powder under high temperature and high pressure [7,8] involves a series of complex processes such as particle translation, turnover, and plastic deformation. In addition, there is also a hot working process involving significant compression and complex deformation [9]. Moreover, it is challenging to study the HIP process of powder in real time, and these problems can be solved by numerical simulation [10,11]. With the help of numerical simulation, the test process can be significantly accelerated and the production cost can be reduced. The prediction and analysis of capsule shrinkage deformation by numerical simulation is a hotspot in the research of HIP near-net shape forming technology. With the progress and innovation of technology, titanium alloy powder

metallurgy technology has been applied to load-bearing parts, such as the impeller and rotor of the F-107 engine. It is more widely used in aircraft parts. From the titanium alloy support rod and fuselage pillar of the F-14 fighter, the keel nose of TC4 alloy of the F-15 fighter, to the engine fixing support of the F-18 hornet fighter, the powder metallurgy of the HIP process is widely used. The utilization rate of materials increased from 10%~35% of the casting and forging process to 50%~60%, and the cost is generally reduced by more than 25% [12,13]. Vinci engine on the French Ariane space rocket adopts a liquid hydrogen impeller fabricated of powder metallurgy, which not only reduces the number of parts of the impeller and the production cost, but also improves the propulsion ratio and prolongs the service time of the engine [14,15]. The multi-type powder TC4/TA15 rudder wing frame products developed by the Institute of Aerospace Materials and Technology, have the advantages of high forming accuracy, good surface quality, and reasonable internal defect control. The material properties fully reach the forging level, and the net size of the whole wing reaches 2200 mm [16].

Many scientists have researched the numerical simulation of the HIP technology. You et al. [17] used the Shima model to simulate and compare the HIP forming process of milled and atomized Ti6Al4V powders. The maximum error between the experimental and simulated results is 2.66%. Numerical simulation is accurate and effective in predicting experiments. Xu et al. [18] studied the microstructure and formation mechanism of TC11 powder titanium alloy. The HIP temperature is 930 °C and the holding time is 2 h. The finite element simulation is carried out with Deform3D software. Procopio et al. [19] used the multi particle finite element model (MPFEM) to explore the densification yield surface of a two-dimensional single-size particle set. A single particle discretized by finite element mesh can fully describe contact mechanics and local and global particle kinematics. The hydrostatic pressure and powder's densification process under different friction levels between particles were studied. The isodensity curve in the stress space during densification shows the equivalent shape of the cap cone model, and the slope of the shear failure line is a function of the friction between particles. MPFEM provides the necessary degrees of freedom to allow local non-uniform contact deformation while capturing the statistical characteristics of the powder. Therefore, the model can deal with corners, non-affine motion, particle rotation, and large deformation under high relative density. The corresponding DEM of the discrete element method is only suitable for the case of relative density <0.85. Kohar et al. [10] used the finite element simulation (FEM) method to simulate the HIP process to avoid trial and error methods in product and process development. The finite element simulation of the HIP process requires that the constitutive model can capture various deformation mechanisms in powder densification, such as plasticity and creep. Since the HIP process may last for several hours, the realization of these values needs to be accurate and efficient. They use the finite element software LS-DYNA to simulate the HIP process of the 304/316L stainless steel jacket. Yuan et al. [20] of the University of Birmingham in the United Kingdom assumed the powder was a compressible porous medium. They used the plastic theory finite element model to describe the powder material. The complex casing product was analyzed by numerically simulating the near-net forming process of the titanium alloy TC4 powder. The simulation results were compared with the test results for the deformation and relative density distribution. The errors in each direction of the simulated dimensions are all less than 2%. Lu et al. [21] of Huazhong University of Science and Technology used the modified Robin hyperbolic sine power rate creep model to predict the plastic deformation behavior of Inconel625 alloy powder. The turbine disc parts with complex shapes were formed and combined with the SLS investment mold to manufacture the shape control core. The simulation error of deformation is 3.27%, and the density error is 2.37%. Xu et al. [22] of Beijing University of Aeronautics and Astronautics used MSC.MARC software to study the numerical simulation process of HIP of thin-walled aluminum alloy complex parts, and the numerical simulation results of the characteristic structure error is about 5%. Baccino et al. [23] proposed the ISOPREC forming process system called HIP near-net shape forming technology. Their products, including

blade discs and shaft parts, can be controlled with a forming accuracy of 0.1 mm. Chung et al. [24] introduced the finite element simulation and optimization method into the field of HIP capsule design and proposed the capsule optimization design prototype system. They used Abouaf's constitutive model and his colleagues, adopted the optimization design technology based on the design sensitivity evaluation scheme, and obtained the required cladding structure based on the rectangular target parts through reverse iterative optimization calculation. Wang et al. [25] studied the influence of different thicknesses of capsule on HIP. The shielding effect of the sheath on the force in the process of HIP is noted. The smaller the thickness of the package, the greater the pressure on the powder body. The molten liquid phase inside the powder is extruded and filled into the gap between the powder particles. The irregular solid phases are extruded and self-locking with each other. The liquid phase filled at the junction of the powder particles promotes the bonding of the particles. It improves the welding degree between the particles and the densification degree of the material. Therefore, the tensile strength, yield strength, and elongation after fracture of powder parts can be improved.

The present research shows that it is feasible to predict the powder deformation process in the HIP process and optimize the design of the capsule and die through numerical simulation. However, most previous studies did not consider the effect of initial powder-filling density in the numerical simulation. This parameter is generally set to 65% (100% represents that the material is entirely dense or the theoretical density). Moreover, the set temperature is evenly distributed in the container, which needs to attract more attention, resulting in inevitable errors in predicting the near final forming results [26]. This phenomenon may be related to the non-uniform distribution of density after vibration and the temperature gradient of powder particles in the capsule. To reveal the possible causes of this phenomenon, numerical simulation can be carried out by the finite element method before HIP to study the influence of the alloy powder's initial relative density distribution on its densification process. Numerical simulation by finite element method can not only visually analyze the densification process and stress field distribution of powder but also monitor the deformation of powder in the simulation process and optimize the capsule structure through its deformation [6,20,27]. In most of the research, the target structure is relatively simple or has a small size. This parameter has little effect on the deformation law of powder in the HIP process. It has little effect on its dimensional accuracy and is often classified as an error. However, for complex part structures or large-size parts, this problem has a significant impact on practical production and applications.

In this paper, the HIP process of Ti6Al4V powder is numerically simulated and experimentally studied. The improved Shima model [28,29] describes the powder and studies the thermal-mechanical coupling deformation. The material parameters of Ti6Al4V powder are determined through relevant physical experiments, and the HIP process parameters are determined based on previous research. By comparing numerical simulation with experiments, the powder's densification process and stress distribution of the capsule are analyzed for uniform and non-uniform initial powder distributions. Finally, the feasibility of the simulation method is verified through the sampling analysis of relative density.

2. HIP Experimental Method

The target part is a cuboid; therefore, a cuboid capsule was designed. Before HIP, the steps of capsule design, powder filling, welding, and degassing should be carried out. The structure and size of the capsule are shown in Figure 1. The capsule is fabricated of stainless steel with a wall thickness of 2 mm. There is also a 16 mm diameter degassing hole in the center of the upper cover.

The HIP process follows the steps below:

Step 1: Use alcohol to perform ultrasonic cleaning on the capsule to remove surface oil and other impurities.

Step 2: Weld the upper and lower covers and the side body with argon arc welding.

Step 3: Detect the capsule's leakage to ensure good welder sealing using a Zqj-560 helium mass spectrometer.

Step 4: Fill the powder into the capsule on the VSR-200 aging vibration system. The vibration frequency is 30 Hz and the time is 1 h.

Step 5: Degas the capsule at 700 °C for 7 h until the vacuum degree reaches 10^{-4} Pa. The FJ-620 molecular pump unit system of KYKY company is used in this step.

Step 6: Place the capsule in an HIP furnace and carry out the HIP process at 920 °C and 120 MPa.

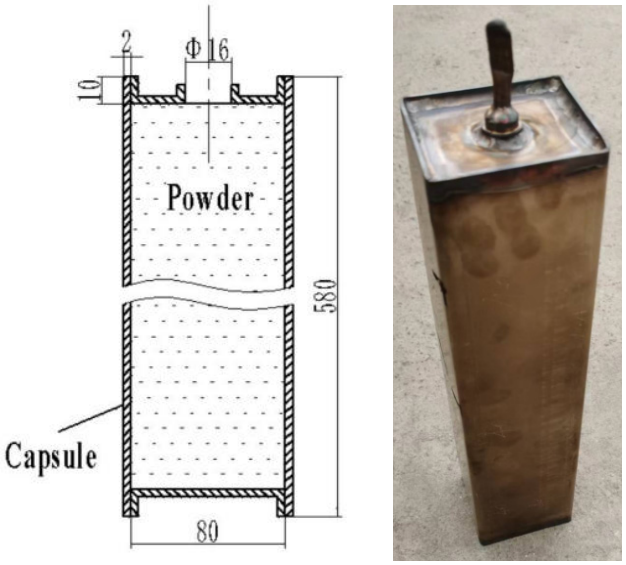


Figure 1. Structural diagram of the capsule and welded one.

The Ti6Al4V pre-alloyed powder used in this paper was purchased from AVImetal company, and the powder particle size is in the range of 53–150 μm, as shown in Figure 2. The chemical composition is shown in Table 1. Figure 3 shows The HIP process route of 920 °C/120 MPa, used for the simulation and HIP experiment.

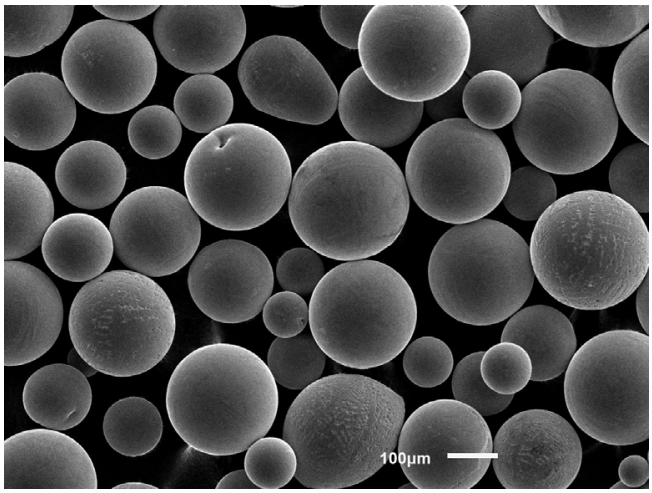


Figure 2. Powder particle morphology.

Table 1. Chemical composition of Ti6Al4V aluminum alloy powders (%).

Ti	Al	V	Fe	O	N	H
bal	6.05	4.21	0.164	0.056	0.006	0.02

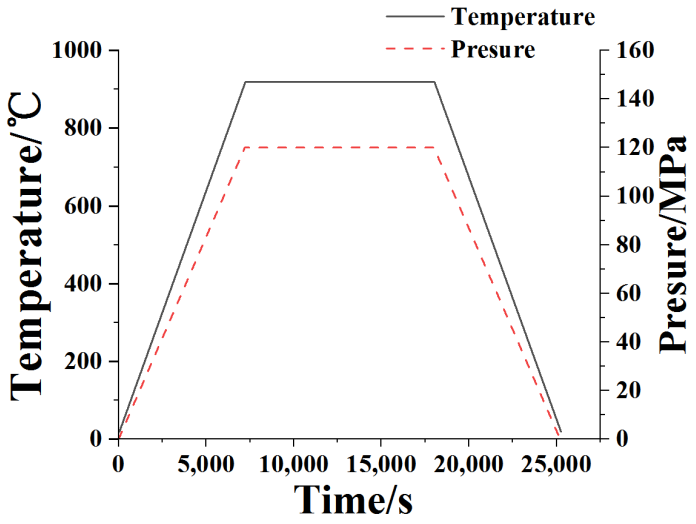


Figure 3. HIP process route.

3. Numerical Simulation

3.1. Mathematical Model

Assuming that the powder is a compressible continuous medium, the classical constitutive equation of continuous medium is modified to obtain the constitutive equation of powder material:

$$\sigma_{eq}^2 = AJ_2^{'} + BJ_1^2 \tag{1}$$

where A and B are parameters related to relative density, J_1 is the first invariant of stress, and $J_2^{'}$ is the second invariant of deviatoric stress.

Shima et al. [28] conducted experiments on copper powder sintered bodies with different densities based on Formula (1) and obtained a yield criterion based on the continuous medium plasticity theory, which is suitable for general metal porous materials. The yield criterion expression is defined as follows:

$$F = \frac{1}{\gamma}\left(\frac{3}{2}\sigma_d\sigma_d + \frac{\sigma_m^2}{\beta^2}\right)^{0.5} - \sigma_y \tag{2}$$

$$\gamma = \left(b_1 + b_2\rho^{b_3}\right)^{b_4} \tag{3}$$

$$\beta = (q_1 + q_2\rho^{q_3})^{q_4} \tag{4}$$

The stress-strain relationship is:

$$d_{\varepsilon_i} = d\lambda\left\{\sigma_i - \left(1 - \frac{2}{9}\beta^2\right)\sigma_m\right\} \tag{5}$$

where γ is the ratio of the nominal flow stress of powder to the actual flow stress of the matrix, β is the influence degree of hydrostatic pressure on the yield surface of the powder. They are all functions of relative density. σ_y is the uniaxial yield stress, σ_m is hydrostatic stress, d_{ε_i} is the principal strain increment, $d\lambda$ is a nonnegative scalar, σ_d is the deviatoric stress tensor, ρ is the relative density, σ_i is the principal stress, and b_1~b_4 and q_1~q_4 are constants, which can be obtained by uniaxial and triaxial compression tests of powder. In addition, we generally use Young's modulus E(T, ρ) and Poisson's ratio V (T, ρ). Such parameters come from various literatures. However, for powder, these parameters change with the relative density of powder [30,31]. Therefore, to improve the accuracy of numerical simulation, it is necessary to obtain the parameters such as Young's modulus

and Poisson's ratio of powder under different densification states. According to the above parameters, Ti6Al4V compact samples with different densities are obtained through the HIP interruption test, and then Ti6Al4V compact samples with different densities are tested at high temperatures.

Hot isostatic pressing is a processing process involving high temperature and high pressure. In this process, the relevant physical parameters of materials change with the temperature change. In the numerical simulation of powder HIP, it is assumed that the physical parameters varying with temperature are independent of the relative density of the dense body. In contrast, Poisson's ratio [30] and elastic modulus of the dense body is calculated by the following formula [32].

$$\nu = \nu_0 \sqrt{\frac{\rho}{3 - 2\rho}} \tag{6}$$

$$E = E_0 \left(0.15 + 0.85\rho^{12}\right) \tag{7}$$

ν_0 is the Poisson's ratio of a fully dense body; E_0 is the elastic modulus of a fully dense body.

At present, other thermophysical parameters involved in the HIP process of titanium alloy powder are usually obtained by experimental method and calculation methods. These two methods have advantages and disadvantages: the data obtained by the experimental method is more accurate than calculation, but the experimental process is complex and time-consuming; the calculation method is simpler, but there are some deviations between the calculated data and the actual value. The physical parameters used in this study are obtained through the HIP interruption test and corrected in combination with the existing literature data [14,33]. The relevant parameters are shown in Table 2.

Table 2. Physical parameters of Ti6Al4V alloy powders.

Temperature (°C)	Modulus of Elasticity (GPa)	Density (g/cm^3)	Heat Capacity Ratio (J/kg·K)	Thermal Expansion System (10^{-6}K^{-1})	Yield Strength (MPa)	Thermal Conductivity (W/m·K)
25	103	4.42	532	8.9	912	15.8
100	99	4.41	551	9.2	725	16
200	94	4.4	573	9.5	610	16.2
300	89	4.38	612	9.7	600	16.4
400	84	4.37	632	9.9	510	17.1
500	80	4.35	751	10.1	330	17.7
600	74	4.34	806	10.3	254	18.2
700	72	4.32	821	10.5	143	19.3
800	70	4.3	902	10.6	120	21.6
900	68	4.28	1105	10.9	100	23.1

3.2. Mesh and Boundary Conditions

The software MSC.MARC is used in this simulation to apply the Shima–Oyane model conveniently. We simplified the model to 1/2 and the mesh consists of two parts, the capsule and the powder, as shown in Figure 4. The hexahedral element is selected for meshing. The model is divided into 29,113 elements, including 4692 capsule elements, and 24,421 powder elements. Then two simulations are carried out. For model I, the initial relative density is set to 65%, which is generally used in previous studies. For model II, the powder part is divided into four gradients from top to bottom, 55%, 60%, 65%, and 70%. The mesh of model I and II are shown in Figure 3. To quantitatively characterize the changes in relevant variables in the HIP process, such as relative density and temperature,

take the sampling lines L1 and L2 shown in Figure 4. The sampling line L2 is half of the thickness of the capsule sample distributed along the xz plane, and the sampling line L1 is the diagonal line of the capsule powder. In the analysis process, we selected seven areas A-G on the sampling line L1. The value of the parameters is the average value of four nodes in the region, and each node on sampling line L2 was selected for data analysis.

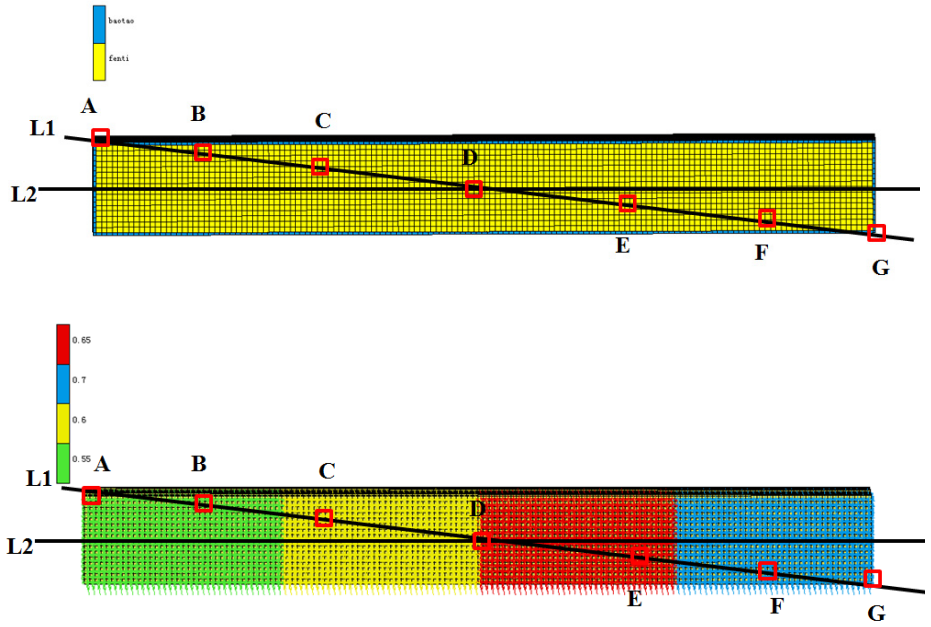


Figure 4. Schematic diagram of grid model and numerical analysis points. A-G are the sampling sites.

This study adopts the heat engine coupling of transient statics using fixed-time step analysis. The modified Newton–Raphson method is selected as an iterative method to solve the nonlinear equations. The displacement is used as the convergence criterion, and the updated Lagrange method is used to describe the large strain problem. Combined with the actual HIP process, the HIP route of synchronous temperature and pressure loading is decided, as shown in Figure 3. The temperature and pressure are increased to 920 °C and 120 MPa at the same time within 7200 s. The temperature is maintained, and the pressure is constant for 10,800 s. At last, it starts to cool down to room temperature and atmospheric pressure within the furnace at 18,000 s. The whole simulation process is 25,200 s or 7 h.

In the HIP process, the value of friction changes following a step function in response to changes in the relative velocity and the increment of the contact displacement between the powder and the capsule. As one of the Coulomb friction model, the stick slip friction model [34,35] reflects the stick slip behavior of the contact surface better. Because of the obvious viscoelastic plasticity of powder under high temperature and high pressure, the stick slip friction model is selected to describe the friction relationship between the powder and the capsule in this study to describe the actual friction phenomenon more precisely [10,36].

4. Discussion

The powder flow is analyzed by displacement vector diagram and history curve of the powder displacement at different times of HIP to analyze the influence of different initial density distributions on the densification process. The densification behavior of the powder is discussed by analyzing the relative density cloud maps of powder at different times and the relative density curves of special nodes. Finally, the simulation results are verified through density testing of the test piece samples.

4.1. Powder Flow Analysis

4.1.1. Simulation Results

Figure 5 shows the displacement vector distributions of the model I at four typical times. Figure 5a shows the displacement vector of the capsule and powder 30 min after the start of HIP. This figure shows that the displacement vectors of the capsule and powder tend to diverge outward simultaneously, mainly moving outward along the axial direction. The reason for this phenomenon is that as the temperature increases, both the powder and the package undergo thermal expansion, and due to the large aspect ratio of the package, the displacement direction is mainly axial. Figure 5b shows the displacement vector after the 2 h HIP process. At this point, the heating and pressure boosting process are completed, the temperature inside the furnace reaches 920 °C and the pressure reaches 120 MPa. At this time, the pressure applied to the capsule is much greater than the material's yield stress, which leads to axial and radial shrinkage of the capsule and powder. Figure 5c shows the displacement vector at the end of the insulation and pressure-maintaining process 5 h after HIP. At this point, the densification process and powder flow of HIP are basically finished, and the package undergoes significant deformation compared with the start of HIP. The overall length is shortened, and the side walls are inward concave. The powder also shows the same flow trend, and the relative density increases, basically achieving densification. Figure 5d shows the displacement vector after HIP. The figure shows that the final shape of the capsule is almost the same as the shape shown in Figure 5c, but the overall displacement increases. This is because in the unloading stage of temperature and pressure, the thermal creep of the powder continues, and the powder and the capsule further shrink due to thermal expansion, finally realizing the densification of the powder.

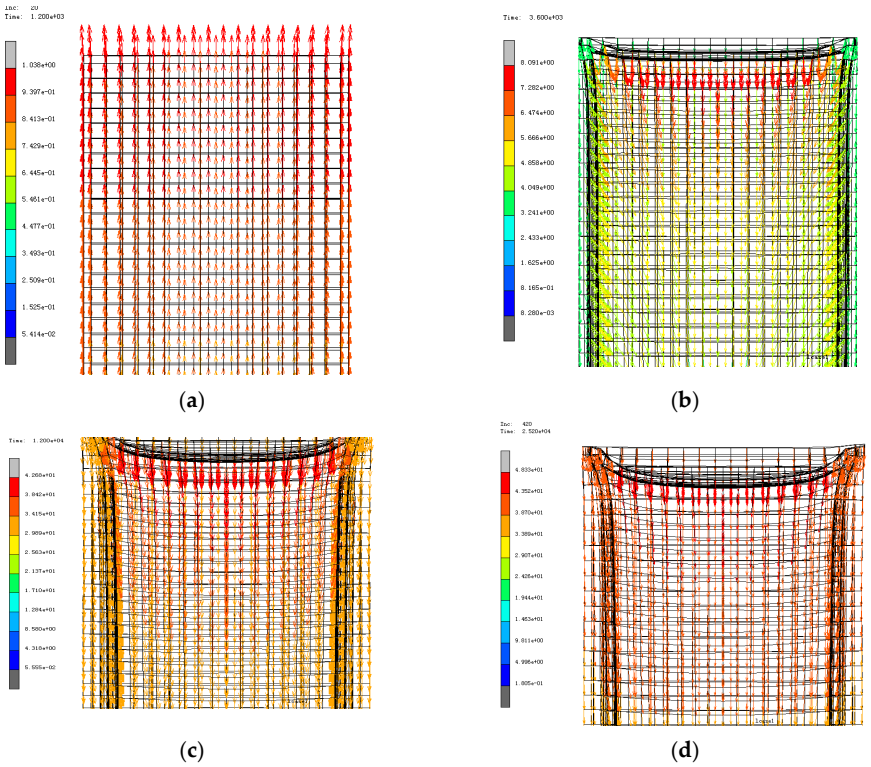


Figure 5. Displacement vector distributions of model I at different times. (**a**) Displacement vector distributions at 30 min; (**b**) Displacement vector distributions at 2 h; (**c**) Displacement vector distributions at 5 h; (**d**) Displacement vector distributions at 7 h.

For model II, the basic flow law of powder is consistent with model I. In Figure 6b, the powder is deformed. By comparing Figures 5d and 6, it can be concluded that the radial shrinkage of different initial density areas is significantly different. The higher the initial

density, the smaller the deformation. The pressure applied to the capsule exceeded the yield strength of the capsule, and the capsule underwent significant plastic deformation. It can be seen from the displacement program that the displacement of each node is large. At the same time, due to the large deformation of the capsule, the upper mold is also dragged to the central area, which is reflected in the displacement vector diagram, that is, all nodes move towards the central area of the powder. At the same time, in the later stage of HIP, during the unloading process of temperature and pressure, the shrinkage effect between the powder and the package occurs due to the decrease in temperature, resulting in the powder's densification.

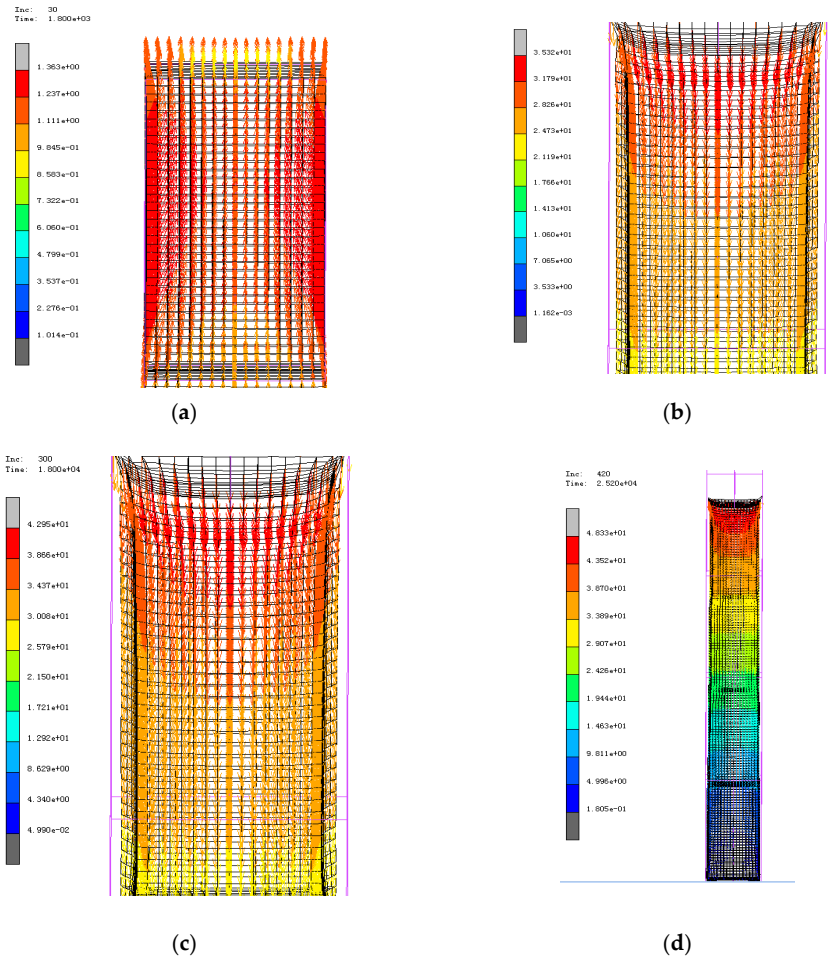


Figure 6. Displacement vector distributions of model II at different times. (**a**) Displacement vector distributions at 30 min; (**b**) Displacement vector distributions at 2 h; (**c**) Displacement vector distributions at 5 h; (**d**) Displacement vector distributions at 7 h.

To characterize the fluidity of powder more accurately, take A-G 7 nodes along L1 in models I and II to analyze the displacement of powder. The sampling line L1 and nodes A-G are shown in Figure 4. The results are shown in Figure 7. It can be seen from Figure 7a that all nodes flow outward due to the effect of thermal expansion at the beginning of HIP. Then, with the continuation of the HIP process, the powder began to shrink, the displacement increased, and the deformation of each node from top to bottom decreased gradually. The displacements of nodes A and B are almost the same, mainly due to the large overall length–diameter ratio of the model. For points A and B on the top, it is mainly the axial size powder shrinkage. For the F and G nodes at the bottom, the deformation of the G point at the bottom is slightly larger than that of F, which is due to the small deformation of the powder due to the "corner effect" of the bottom corner capsule. A similar displacement trend of the powder can also be observed in Figure 7b. Compared with model I, the

displacement difference between the A and B nodes of model II is larger. In addition, the overall displacement of corresponding nodes of model II is smaller than that of model I. This is mainly due to the uneven initial distribution of the powder, which leads to part of the powder being in a state of unidirectional loading, which is not conducive to the flow of the powder. Similarly, for the F and G nodes at the bottom, the situation is similar to Figure 7a due to the corner effect.

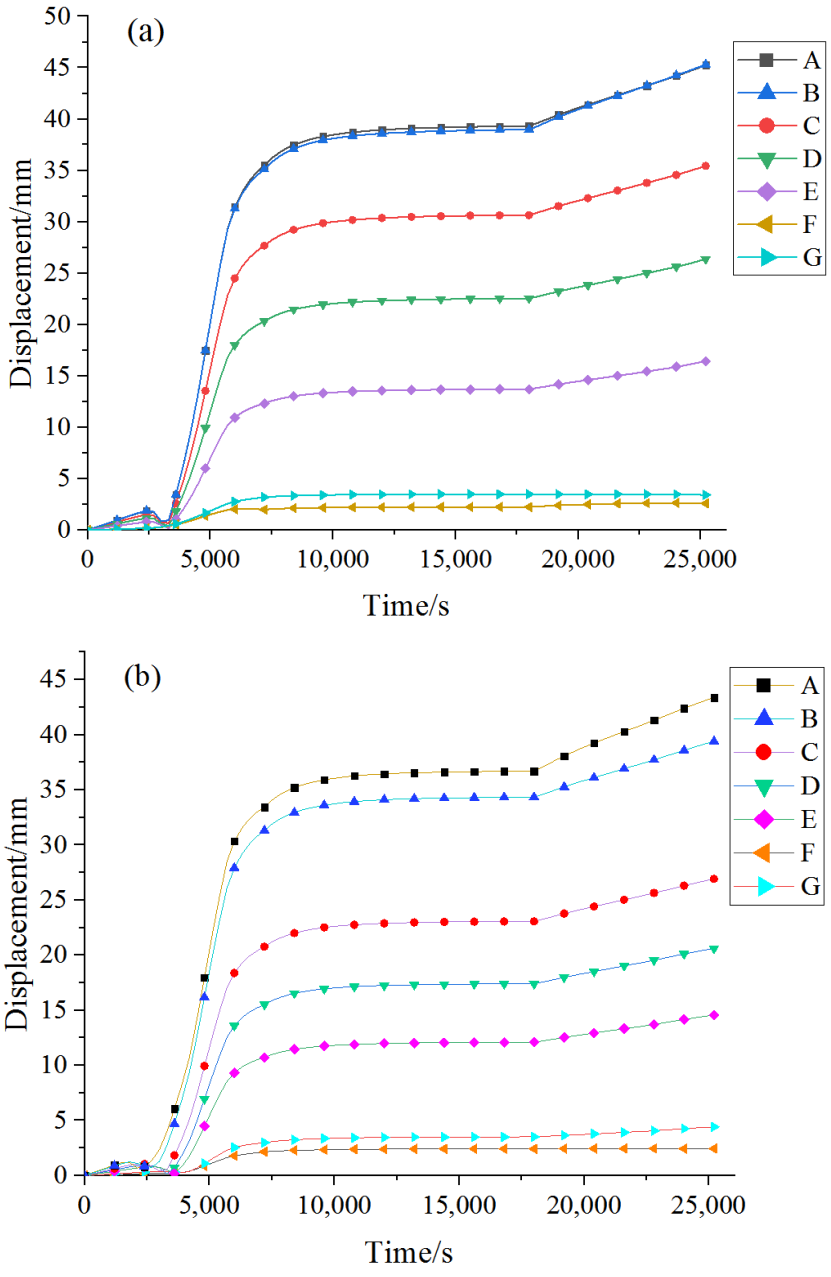


Figure 7. Displacement histories of model I and model II at different locations of test line L1. (**a**) Displacement histories of model I. (**b**) Displacement histories of model II.

Figure 8 shows that under the two simulation cases, the overall deformation trend of the powder body is the same, which is axial contraction and contracted from the left and right sides to the middle in the radial direction. The difference is that in simulation I, the radial shrinkage is almost the same and evenly distributed except for the top and bottom, and the shrinkage of radial direction is 5.1 mm. However, in simulation II, due to the uneven distribution of initial density, the radial shrinkage is also different and gradually

decreases from top to bottom. To specifically analyze the shrinkage of different parts, four points are chosen outside the powder from four densities to draw the history curves of deformation which are shown in Figure 9.

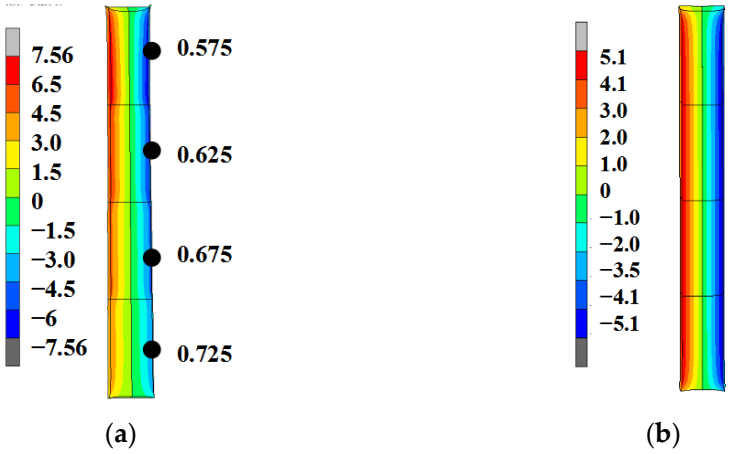


Figure 8. Radial displacement of simulation I and II. (**a**) simulation I; (**b**) simulation II.

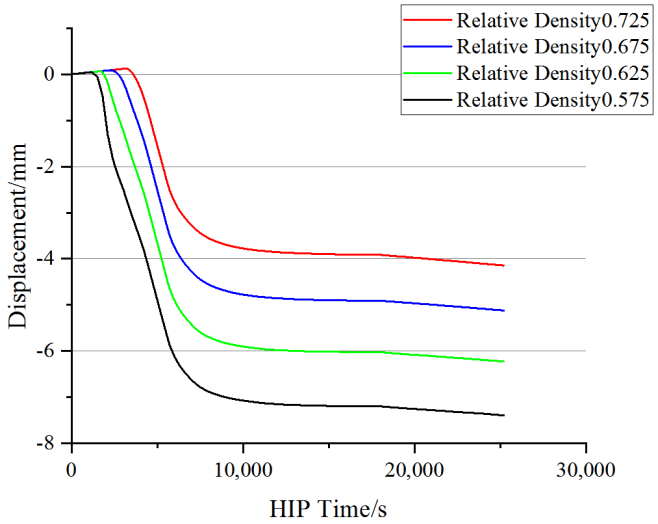


Figure 9. Displacement of histories of simulation II.

4.1.2. Experimental Results

It can be observed from Figure 6 that with the gradual increase in pressure, the powder begins to densify and shrink and drives the capsule to shrink and deform together. At the end of HIP, the deformation of the four nodes is significantly different. The final deformation of the node with an initial density of 57.5% is the largest, reaching 7.5 mm. In comparison, the deformation of the node with an initial density of 72.5% is only about 4 mm. The capsule is cut and measured to verify the accuracy of simulation I and II and explore the actual shrinkage of experimental powder parts. The measuring method is shown in Figure 10. The capsule is cut at the selected position corresponding to four different densification regions and then the length of the deepest pit in the middle was measured. The obtained data are shown in Table 3. The numerical simulation results are also shown in Table 3 to compare with the experiment results. The relative error δ is calculated according to Formula (6), where L is the experimental size, and $\mathcal{L}$ is the numerical simulation size.

$$\delta = \frac{\Delta}{\mathrm{L}} = \frac{|\mathcal{L} - \mathrm{L}|}{\mathrm{L}} \times 100\% \tag{8}$$

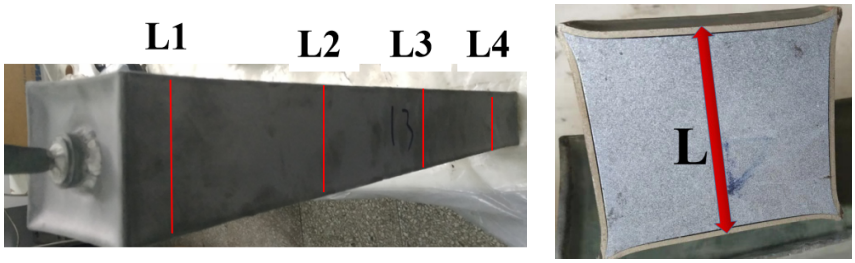


Figure 10. Schematic diagram of dimension measurement after HIP.

Table 3. Comparison of experimental and simulated size.

	L1	L2	L3	L4
Initial size/mm		80		
Experiment size/mm	65.9	67.2	68.5	69.6
Simulation I size/mm		68.7		
Simulation II size/mm	64.4	67.6	69.7	71.8
Relative error of experiment I	4.2%	2.23%	0.29%	1.29%
Relative error of experiment II	2.27%	0.59%	1.75%	3.16%

The data in Table 3 indicate that the radial shrinkage in different capsule parts differs after HIP. For this experiment, when the initial relative density value is set to 65%, the same as most research to describe the initial distribution state of powder, the final result produces a maximum relative error of 4.2%. When the initial powder density is subdivided according to the gradient, the maximum error is only 3.16%. Further analysis shows that the position with the most significant error is the block with an initial density of 70%. In fact, even if the vibration system is used as assistance in the powder-filling process, it is impossible to achieve such a high density. Therefore, if this value is properly reduced, the accuracy of the final numerical simulation is improved. At the same time, it also shows that in the actual HIP powder-filling step, the actual distribution state of powder density may be more complex, and further research is needed.

4.2. Densification Analysis

The density of the powder is an essential index of the forming quality of powder HIP. Numerical simulation can dynamically reflect the relative density distribution at different times in the process of HIP. Therefore, the law of their densification process is explored by analyzing the relative density changes during the HIP process of the two models.

4.2.1. Simulation Results

Figure 11 shows the relative density distribution of model I. For model I, the initial relative density of the powder is set to 65%. However, from Figure 11a, it can be seen that shortly after the start of HIP, the relative density of the powder does not increase but decreases, dropping to around 61~64%. This is because during this stage, the thermal expansion effect caused by temperature rise dominates, and the overall outward expansion of the powder leads to a decrease in relative density. As the HIP process continues, the capsule and powder particles soften with the increase in temperature. The force exerted by the deformation of the capsule on the internal powder causes significant plastic deformation of the powder particles, and the density of the powder gradually increases, as shown in Figure 11b,c. At this point, the maximum relative density of the powder reached 97%. The overall densification of the part is relatively uniform under this process. When the HIP ends, as shown in Figure 11d. The relative density of the powder body reached a maximum of over 98%, basically achieving densification.

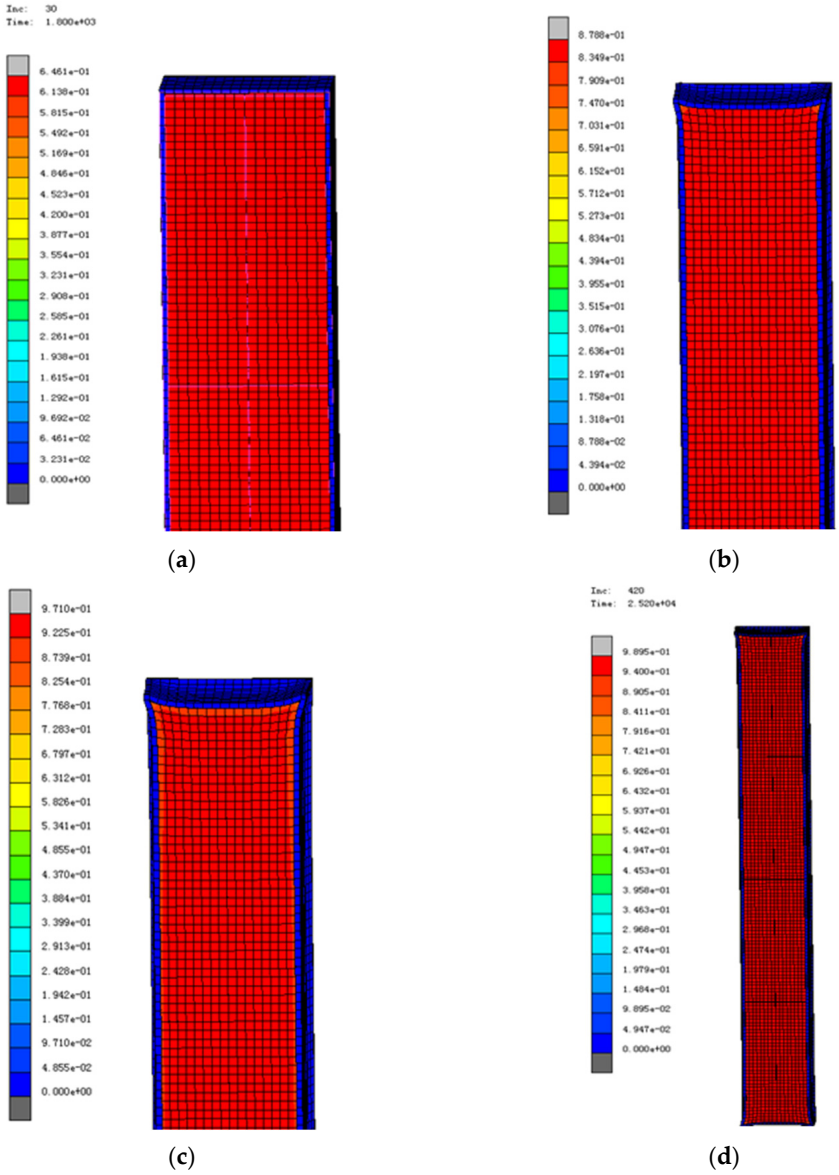


Figure 11. Relative density distributions of model I at different times. (**a**) Relative density distributions at 30 min; (**b**) Relative density distributions at 1 h; (**c**) Relative density distributions at 4 h; (**d**) Relative density distributions at 7 h.

The initial density of model II is divided into four parts from 55% to 75%. As seen in Figure 12a, there is a process of relative density reduction in the early stage of HIP. This is because, in the initial stage, the extrusion effect of low isostatic pressure on the capsule is less than that caused by the thermal expansion effect of the powder in the capsule due to the increase in temperature, resulting in the reduction in the relative density of the powder. This stage lasts for a short time and has little impact on the whole. As shown in Figure 12b, with the increase in pressure and temperature, the relative density of powder presents a rapidly rising stage. In this stage, the relative density of powder increases rapidly from the original 55% to more than 85% and enters the thermal insulation and pressure holding stage. This is because, with the increase in temperature and pressure, the capsule deforms under high pressure to drive the rapid flow of internal powder particles. In addition, with the increase in temperature and pressure, the driving force of the powder exceeds the yield strength of the alloy powder particles, and the powder particles produce obvious plastic deformation and squeeze the internal pores. When the HIP process enters the later stage of heat preservation and pressure holding, as shown in Figure 12c, although the

compactness of the powder body improved, the increasing rate is low. At this stage, the plastic deformation of the powder particles reached the saturated state, and the powder particles have been interconnected as a whole. At this time, the slow densification behavior mainly depends on the diffusion and creep effects. Compared with model I, there are apparent differences in the density boundary of the four parts initially divided.

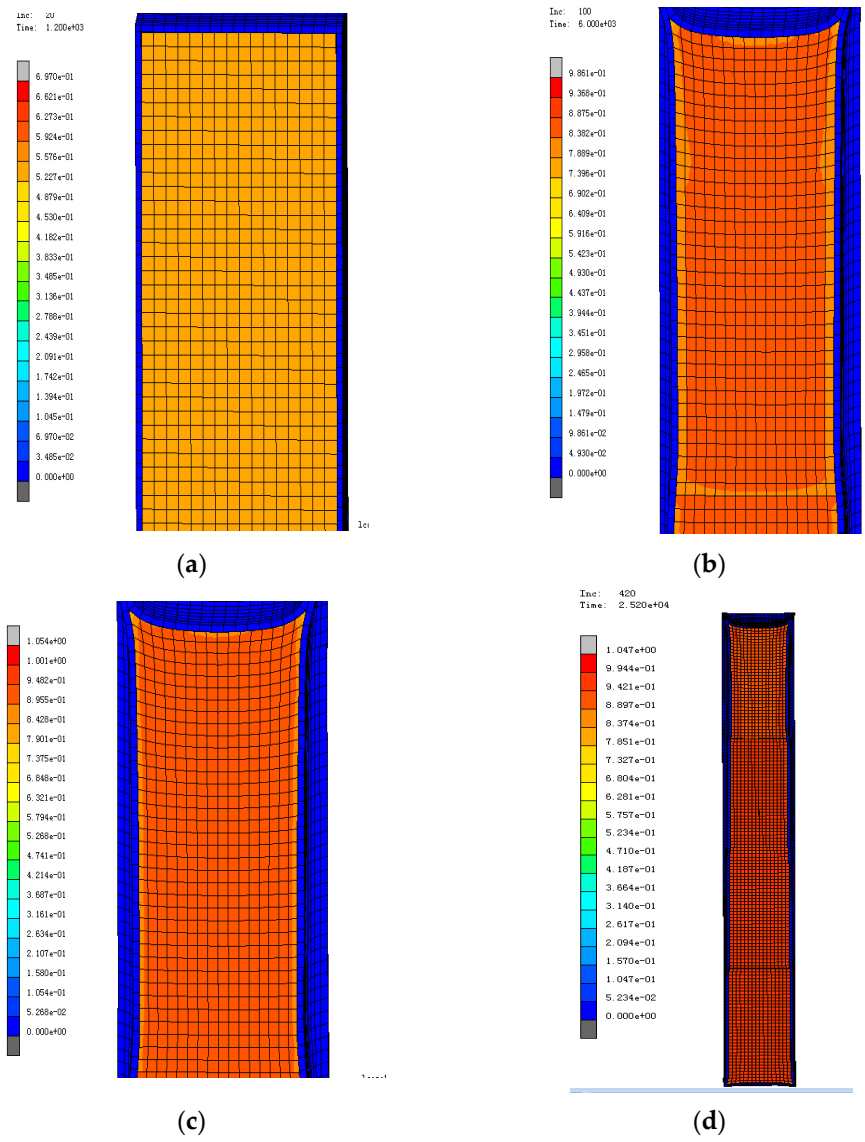


Figure 12. Relative density distributions of model II at different times. (**a**) Relative density distributions at 30 min; (**b**) Relative density distributions at 1 h; (**c**) Relative density distributions at 4 h; (**d**) Relative density distributions at 7 h.

To study the densification process of powder in the HIP process more accurately, seven nodes are taken along test line L1, as shown in Figure 3 and the density of corresponding nodes is analyzed.

Figure 13 shows the distribution of the relative density of characteristic nodes on test lines L1 after HIP. It can be concluded from Figure 13a that the relative density of all nodes of sampling line L1 increases steadily with the extension of time. At a specific time, the relative density of all nodes of sampling line L1 is almost the same. However, the relative density of nodes close to the upper and lower covers is smaller. In comparison, the relative density of nodes located in the center of the powder body is higher. After HIP, the relative density of powder in the capsule is more than 95%. It can be seen from Figure 13a

that the change curve of relative density has a process of relative density reduction in the early stage of HIP. Because, in the initial stage, the isostatic pressure on the capsule is less than that of the powder in the capsule due to the thermal expansion effect caused by the increase in temperature, resulting in the reduction in the relative density of the powder. This stage lasts for a short time and has little impact on the whole. With the increase in pressure and temperature, the relative density of powder presents a rapidly rising stage. In this stage, the relative density of powder increases rapidly from the original 65% to more than 85%, and enters the thermal insulation and pressure holding stage. This is because, with the increase in temperature and pressure, the capsule deforms under high pressure to drive the rapid flow of internal powder particles. In addition, with the increase in temperature and pressure, the capsule driving force of the powder exceeds the yield strength of the alloy powder particles, and the powder particles produces obvious plastic deformation and squeezes the internal pores. When the HIP process enters the later stage of heat preservation and pressure holding, although the compactness of the powder body improved, the increasing rate is low, because at this stage, the plastic deformation of the powder particles reached the saturated state. The powder particles are interconnected as a whole. At this time, the slow densification behavior mainly depends on the diffusion and creep effects. Figure 13a shows that for model I, the shrinkage of powder at A and G points at the corner of test line L1 is insufficient due to the edge angle effect of cladding, which further leads to the lack of relative density. The relative density of points B and F near the capsule rather than the corner is the highest. Nodes C, D, and E near the center are slightly lower than B and F but higher than 95%. This is because, during the powder densification process, the external powder first undergoes densification and forms a high-density external powder layer, which somewhat hinders the densification of the internal powder body. As shown in Figure 13b, compared with model I, the relative densities of seven nodes of model II differs after HIP. The lowest relative density is at point A at the upper corner, only about 83%. The highest density is the F point at the bottom non-corner, and the final density is as high as 97%. In addition, although the initial relative density has a gap of up to 20%, the final relative density distribution of the B-F point is relatively uniform, controlled within 5%. It can be concluded that the initial relative density of the powder compact has little effect on the overall densification of the powder body and is consistent with the initial density distribution of the uniform state. The final density distribution is consistent with the previous analysis of powder fluidity.

Figure 14 shows the relative density of nodes on the sampling line L2 at different times in model I. The relative density of the nodes on line L2 in the first 30 min of HIP was an overall decline due to thermal expansion, which was only 63%. With the HIP process, the relative density increases rapidly to about 85%, but the top and bottom of the powder are relatively low. It can be seen from the figure that the relative density of all nodes of sampling line L2 increases steadily with the extension of time. At a specific time, the relative density of all nodes of sampling line L2 is almost the same. However, the relative density of nodes close to the upper and lower covers is small, while the relative density of nodes located in the center of the powder body is high. At this time, the powder entered the densification stage due to the slow diffusion of the powder at the later stage of isothermal deformation. After HIP, the relative density of alloy powder in the capsule is about 95%.

Compared with model I, the variation trends of the model are similar, but due to the setting of initial conditions, it is divided into four parts of relative density from 55% to 70%, and there is a large mutation at the interface of different density zones, as shown in Figure 15. The difference between the temperature and the density of the whole powder gradually decreases with the temperature increase. At the end of the HIP process, the overall density increases to about 95%, the density of the four parts of the powder is basically the same, and the gap between the interfaces almost disappears. The overall density of the powder is not significantly affected by the initial density.

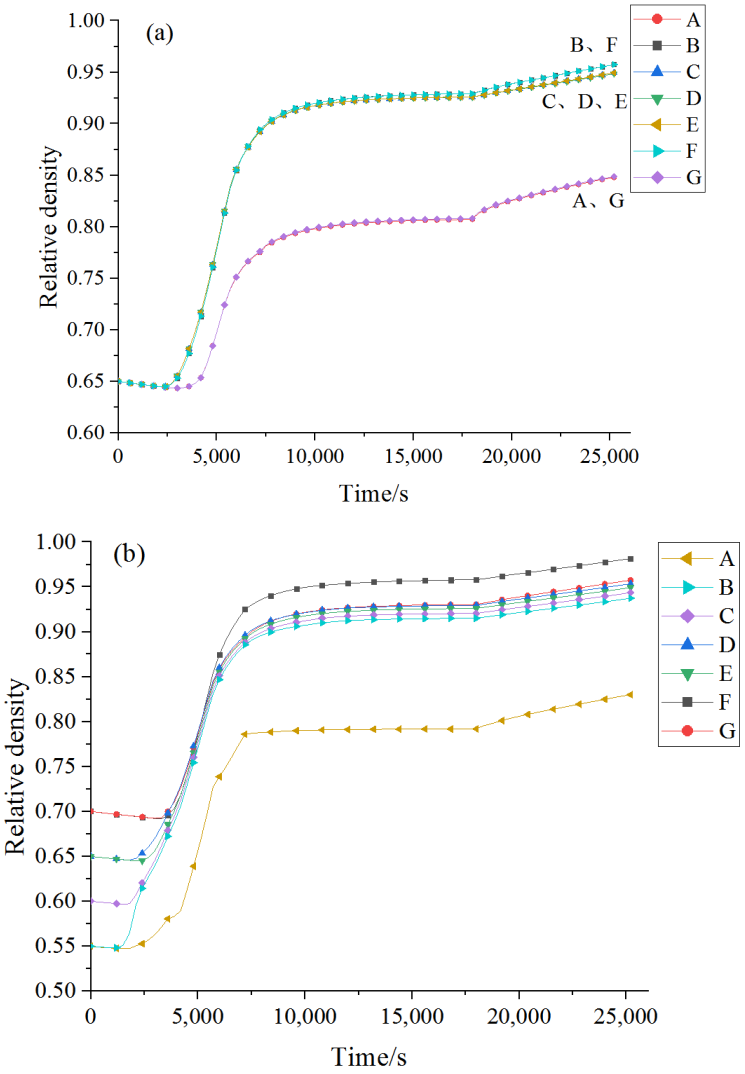


Figure 13. Density change process at test line L1 in model I and II. (**a**) Density change process of model I; (**b**) Density change process of model II.

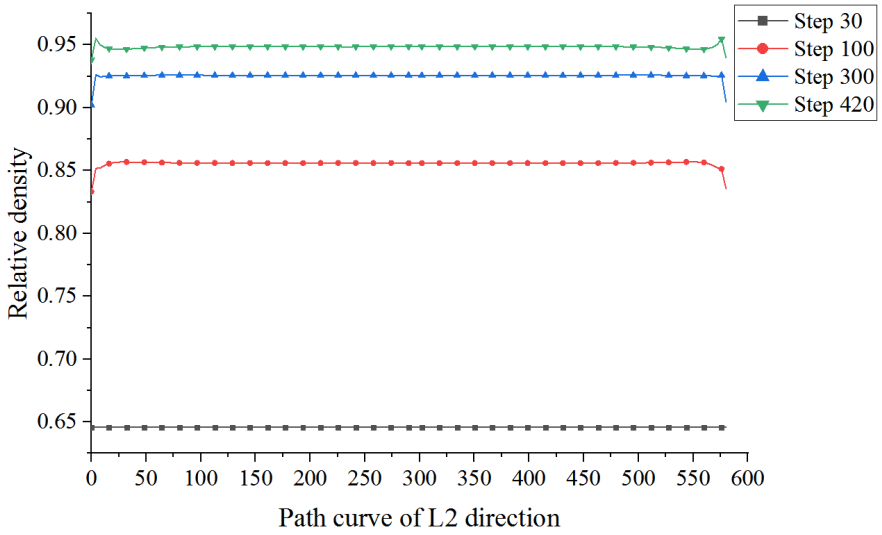


Figure 14. Variation trends of the relative densities of test line L2 of model I.

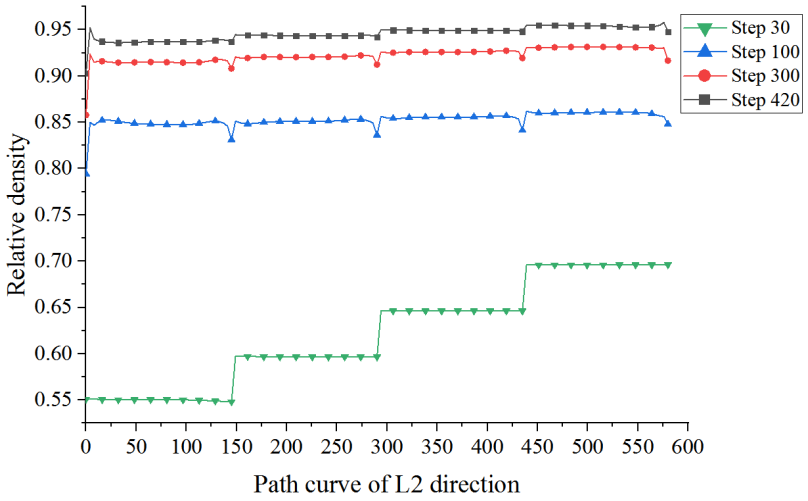


Figure 15. Variation trends of the relative densities of test line L2 of model II.

Figure 16 compares the overall densification process between model I and model II. For the uniform initial powder relative density distribution in model I, and the uneven initial powder relative density in model II, the overall relative density is both 65% at the beginning and about 95% at the end. After the start of HIP, the relative density of the powder in both models showed a brief decrease due to thermal expansion. The non-uniformly distributed model II shows a more significant decrease and lasts longer. This also leads to the overall relative density of model II being lower than model I during the initial stage of powder densification during the HIP process. As HIP progresses, the overall density of model II reverses that of model I. This indicates that the non-uniform distribution of the initial relative density of the powder has specific benefits for improving the final density of the powder.

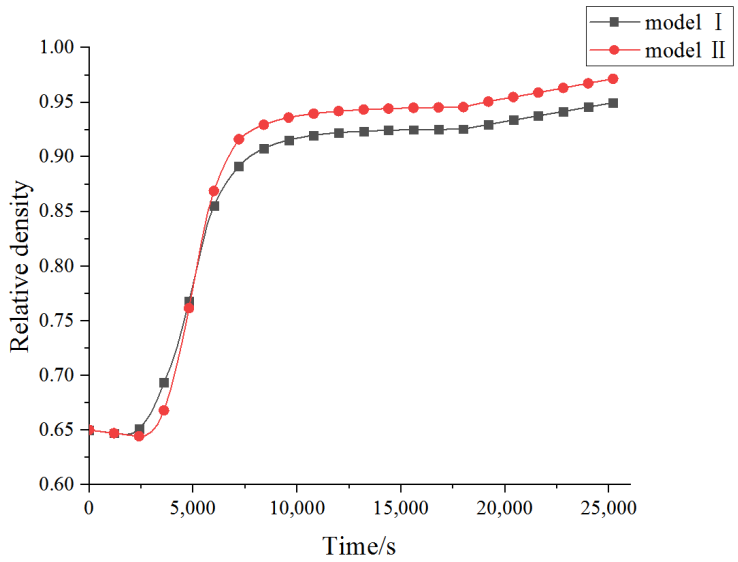


Figure 16. Comparison of the overall densification trends of model I and model II.

Figure 17 shows the final densification results of parts under different initial density conditions. Figure 17a shows the distribution of final Mises stress when the initial density distribution is uniform. Figure 17b shows the final densification degree and Mises stress distribution when the initial density distribution is non-uniform. It can be seen that since the initial density of the upper part of the capsule is less than that of the lower part, the upper part of the capsule has greater volume shrinkage after HIP, and the final densification

degree of the upper part is lower than that of the lower part of the capsule. There is an obvious interface at the boundary of the initial density, and the original interface has no continuous transition after superheated isostatic pressing. In the final formed parts, these places of density discontinuous transition become the places of crack initiation, which should be avoided as much as possible. Due to the non-uniform distribution of initial density, the deformation degree of the capsule is different from the distribution of stress. From top to bottom, shear action occurs in the powder due to the plastic deformation of the cladding, and the powder particles produce corresponding internal force to resist this action. In the capsule with uniform initial density distribution, due to the uniform plastic deformation of the package as a whole, the resistance generated in the particle is smaller, and the Mises yield stress distribution is more uniform. The above comparative analysis shows that the higher the initial relative density, the final parts with a higher degree of densification are obtained under the same HIP process. The more uneven the initial relative density distribution, the more plastic deformation of the package occurs. The shear effect caused by the non-uniform deformation makes the internal resistance stress generated in the powder greater and the powder particles easier to break.

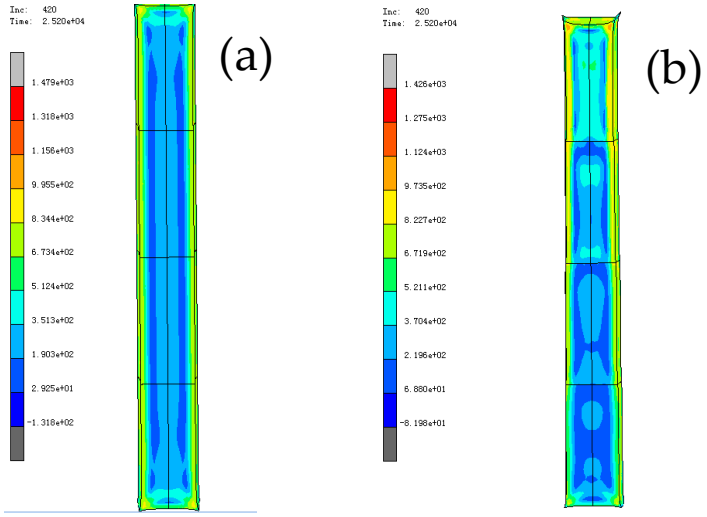


Figure 17. The Mises stress distribution of the powder: (**a**) Uniform initial density distribution, (**b**) non-uniform initial density.

As shown in Figure 18 in the process of HIP, the high-pressure gas in the HIP furnace does not directly act on the powder but drives the internal powder to be dense through the plastic deformation of the capsule, that is, the isostatic pressure applied in the hip process is transmitted to the powder through the deformation of the capsule. Because of the uneven distribution of the temperature field of the powder and the uneven deformation of the internal particles, the deformation and stress distribution of the package with the deformation of the powder are also uneven. It can be seen from the comparison of the distribution of stress at the boundary of model I and model II in the whole package that the distribution of stress at the boundary of model I is more uniform, which is also consistent with that at the boundary of model II. A more significant stress concentration may exceed the strength limit of the cladding material and cause the capsule to crack.

To provide a more detailed study of the magnitude and evolution law of equivalent Cauchy stress in the two models, as shown in Figure 18, select three points ABC at the corner, side, and plane of the capsule. The stress change during HIP is analyzed. The variation curve of equivalent Cauchy stress of the node with time is shown in Figure 19. In the initial stage of the HIP process, the capsule expands outward due to heating and deforms, but the point A at the corner of the capsule is not deformed due to the influence of the edge angle effect. With the increase in temperature and pressure exceeding the yield strength of the capsule, the capsule undergoes plastic deformation and begins to shrink

inward. The equivalent Cauchy stress at the three nodes rises rapidly, consistent with the billet's relative density growth curve in the figure. After entering the thermal insulation and pressure holding stage, the density of the powder is greatly improved, and the densification and deformation speed is greatly reduced, reducing the shrinkage rate of the cladding. The compressive stress is equivalent to the yield strength of the cladding material at this temperature; therefore, the Cauchy stress is basically maintained in a stable state. When the HIP working condition enters the unloading stage, the temperature and pressure begin to decrease uniformly, resulting in an upward trend of the equivalent Cauchy stress at the three nodes. As the temperature approaches the ambient temperature, the plastic strain increment in this stage is 0. A sizeable residual stress is finally generated because of different materials' different thermal expansion coefficients. Upon comparing Figure 19a,b, it can be found that the variation trend of the equivalent Cauchy stress of the three nodes under the two models is basically the same, but for model II, which is Figure 18b, the stress variation in point C, the interface of the area with uneven initial density distribution, fluctuates wildly. This is because the uneven initial density distribution of the powder leads to the uneven deformation of the capsule, the uneven stress distribution and sudden change at a specific time, which increases the fracture risk of the capsule.

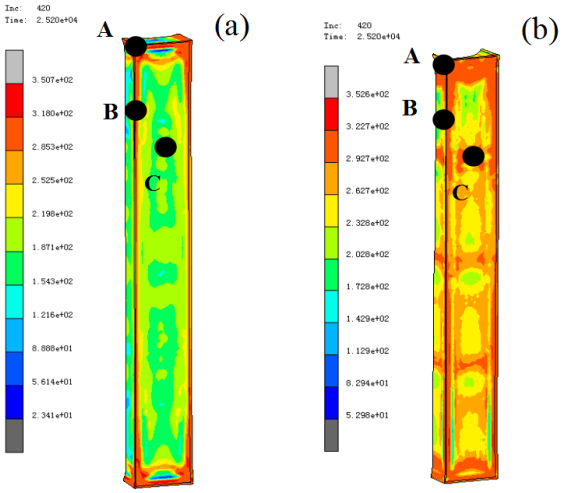


Figure 18. The stress distribution of the capsule: (**a**) uniform initial density distribution, (**b**) non-uniform initial density. A–C are the sampling points.

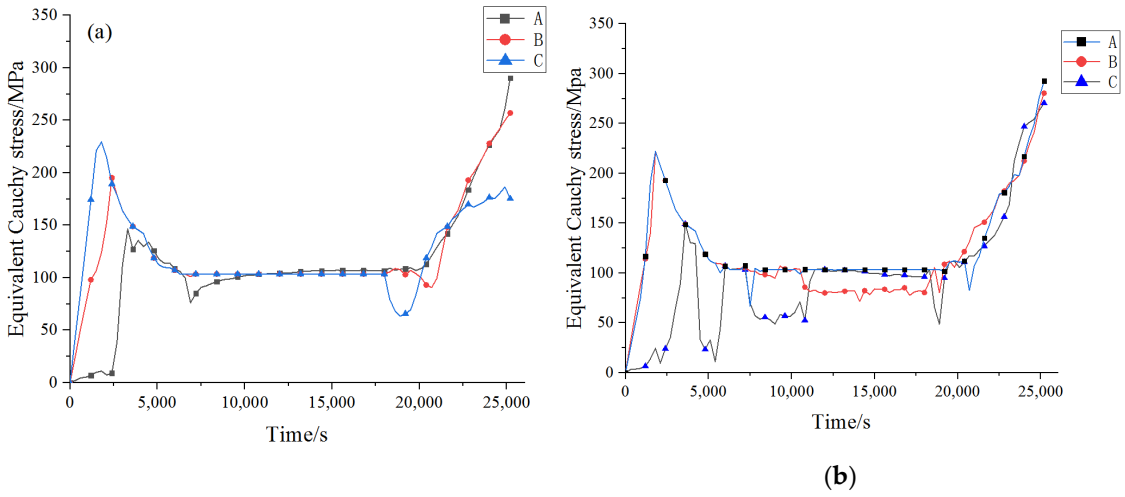


Figure 19. Variation diagram of equivalent Cauchy stress of each node. (**a**) Uniform initial density; (**b**) Non-uniform initial density.

4.2.2. Experimental Verification of Simulation Results

Firstly, the capsule is cut along L1-L4, as shown in Figure 10. Then, the samples are taken at point A, B, and C as shown in Figure 20. The sample size is 5 × 5 × 3 mm. Then, with the PUCHUN-JA103 electronic balance, the sample density is measured using the drainage method and the relative density is calculated. The data of measured relative density and simulation results are shown in Table 3.

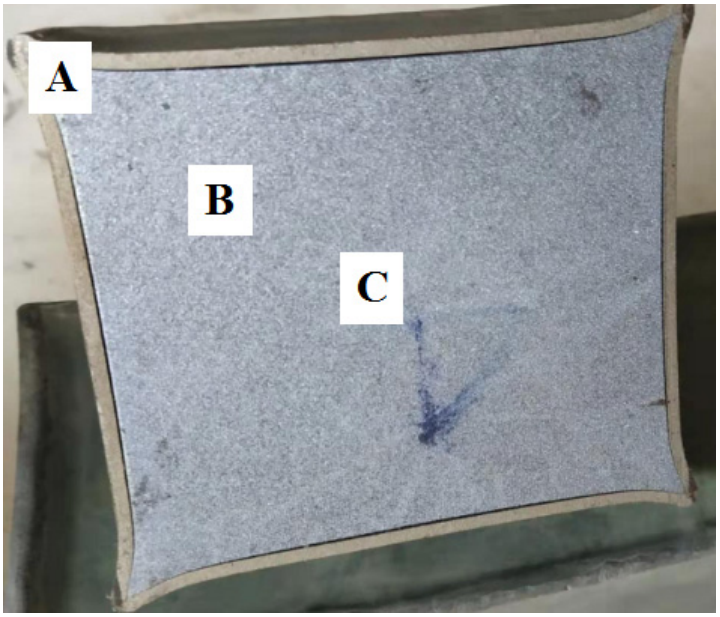


Figure 20. Schematic diagram of sampling location. A–C are the sampling sites.

It can be concluded from Table 4 that, in general, the numerical simulation results are roughly the same as the experimental results, and the relative density error is within 5%. The relative density of regions B and C reaches more than 95%, and the error between them and the numerical simulation results is acceptable. The relative density of zone A is only about 0.85, mainly due to the influence of the corner effect at the sharp corner. It reduces the fluidity of the powder and hinders the densification of the powder. Figure 21 shows the A part's microstructure, where some powder particles have been sintered and merged, but there are some pores between the particles. This is consistent with the conclusion of the previous analysis. On the whole, the relative density of the numerical simulation is lower than the actual relative density. This is mainly because the macro finite element modeling ignores the cavity collapse process caused by particle translation in the early stage of the HIP. At the same time, the current macro simulation needs to be improved for the increase in powder density caused by diffusion creep in the later stage of HIP. Comparing the results of the model I and model II, it can be found that assuming that the initial density distribution of powder is uniform, the relative density of the same nodes of simulation I at four different sections is basically the same. The experimental results show that the relative density of different sections at the same position is different, and simulation II with different initial densities has the same characteristics and the relative error with the actual results is smaller. This is because in the process of powder filling, due to the uneven vibration, the relative density of the powder at the bottom of the package is greater than that at the upper part. In the area closer to the powder loading hole, due to the welding requirements and the powder thrown out by vibration, the relative density of this part of the powder is lower. Further analysis shows that the initial relative density distribution of the actual powder is more complex than that, gradually increasing from top to bottom.

Table 4. Comparison of experimental and simulated relative density.

	Experiment	Simulation I	Relative Error	Simulation II	Relative Error
A1	0.845	0.824	2.5%	0.821	2.8%
A2	0.862	0.827	4.1%	0.825	4.3%
A3	0.856	0.827	3.4%	0.833	2.7%
A4	0.875	0.827	5.5%	0.842	3.8%
average			3.9%		3.4%
B1	0.953	0.933	2.1%	0.925	2.9%
B2	0.958	0.935	2.4%	0.938	2.1%
B3	0.967	0.935	3.3%	0.947	2.1%
B4	0.969	0.935	3.5%	0.954	1.5%
average			2.83%		2.2%
C1	0.966	0.946	2.1%	0.935	3.2%
C2	0.971	0.946	2.6%	0.942	2.9%
C3	0.973	0.946	2.8%	0.95	2.4%
C4	0.982	0.946	3.7%	0.955	2.7%
average			2.8%		3.5%

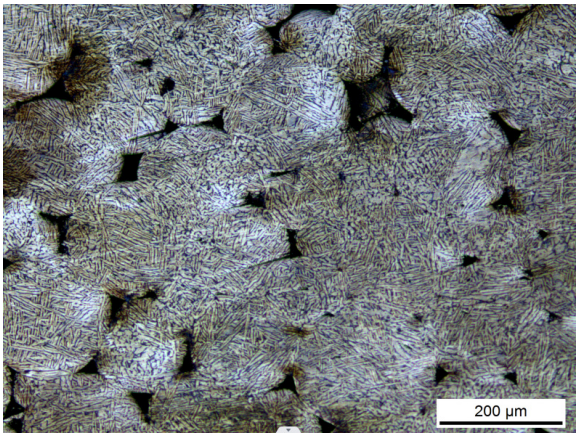


Figure 21. Microstructure of A part.

5. Conclusions

1. The radial shrinkage of capsule parts with a large aspect ratio significantly differs after HIP. This is mainly due to the inhomogeneous distribution of powder density during the initial powder-filling process.
2. A method for Ti6Al4V HIP simulation considering the non-uniform distribution of initial powder filling was developed. This method can effectively improve the accuracy of numerical simulation. The maximum relative error of the final displacement result is reduced from 4.2% to 3.16%.
3. In the non-uniform initial powder distribution model, the initial density boundary exhibits a clear interface after HIP, and there is no continuous transition at the original interface after HIP. For the stress distribution, the deformation degree of the capsule is different due to the non-uniform initial density distribution, which increases the risk of capsule rupture. For the HIPed parts, these density discontinuous transition areas become the initiation of crack. This is also one of the reasons for the poor fatigue performance of HIP parts.

In this paper, the effects of non-uniform distribution on the HIP process are analyzed. It provides an improved method or parameter to make the numerical simulation more accurate, especially for near-net shaping of the HIP process. However, it should be noted that in practical engineering applications, the initial distribution of powder is much more complex than in this experiment. Further studies are needed to extend the method to a more realistic distribution state.

Author Contributions: Conceptualization, L.L.; Methodology, F.M.; Project administration, L.L.; Software, F.M.; Writing—original draft, F.M.; Writing—review and editing, Y.X. All authors have read and agreed to the published version of the manuscript.

Funding: This research received no external funding.

Data Availability Statement: Data available on request due to restrictions e.g., privacy or ethical. The data presented in this study are available on request from the corresponding author. The data are not publicly available due to privacy.

Conflicts of Interest: The authors declare no conflict of interest.

References

1. Bocanegra-Bernal, M.H. Hot Isostatic Pressing (HIP) technology and its applications to metals and ceramics. *J. Mater. Sci.* **2004**, *39*, 6399–6420. [CrossRef]
2. Fang, Z.Z.; Paramore, J.D.; Sun, P.; Chandran, K.S.R.; Zhang, Y.; Xia, Y.; Cao, F.; Koopman, M.; Free, M. Powder metallurgy of titanium–past, present, and future. *Int. Mater. Rev.* **2018**, *63*, 407–459. [CrossRef]
3. AlHazaa, A.; Haneklaus, N. Diffusion Bonding and Transient Liquid Phase (TLP) Bonding of Type 304 and 316 Austenitic Stainless Steel—A Review of Similar and Dissimilar Material Joints. *Metals* **2020**, *10*, 613. [CrossRef]
4. Chai, L.; Tassou, S.A. A review of printed circuit heat exchangers for helium and supercritical CO2 Brayton cycles. *Therm. Sci. Eng. Prog.* **2020**, *18*, 100543. [CrossRef]
5. Nakatani, M.; Masuo, H.; Tanaka, Y.; Murakami, Y. Effect of Surface Roughness on Fatigue Strength of Ti-6Al-4V Alloy Manufactured by Additive Manufacturing. *Procedia Struct. Integr.* **2019**, *19*, 294–301. [CrossRef]
6. Xue, P.J.; Wu, Y.; Huang, J.; Wei, Q.S.; Shi, Y.S.; Yan, C.Z. Near Net Shape Forming Process of a Titanium Alloy Component Using Hot Isostatic Pressing with Graphite Mould. *Appl. Mech. Mater.* **2014**, *599–601*, 81–87. [CrossRef]
7. Atkinson, H.V.; Davies, S. Fundamental Aspects of Hot Isostatic Pressing: An Overview. *Metall. Mater. Trans. A* **2000**, *31*, 2981–3000. [CrossRef]
8. Seop, K.H. Densification mechanisms during hot isostatic pressing of stainless steel powder compacts. *J. Mater. Process. Tech.* **2002**, *123*, 319–322.
9. Guo, R.; Yu, B.; Shi, X.; Xu, L.; Yang, R. Effect of Powder Size on Fatigue Properties of Ti-6Al-4V Powder Compact Using Hot Isostatic Pressing. *JOM* **2019**, *71*, 3614–3620. [CrossRef]
10. Kohar, C.P.; Martin, É.; Connolly, D.S.; Patil, S.; Krutz, N.; Wei, D.; Inal, K. A new and efficient thermo-elasto-viscoplastic numerical implementation for implicit finite element simulations of powder metals: An application to hot isostatic pressing. *Int. J. Mech. Sci.* **2019**, *155*, 222–234. [CrossRef]
11. Redouani, L.; Boudrahem, S.; Alem, S. New hot isostatic pressing (HIP) simulation method with taking into account of the operating cycle ramp. *Int. J. Adv. Manuf. Technol.* **2019**, *102*, 3291–3299. [CrossRef]
12. Chen, G.L.; Xu, X.J.; Teng, Z.K.; Wang, Y.L.; Lin, J.P. Microsegregation in high Nb containing TiAl alloy ingots beyond laboratory scale. *Intermetallics* **2007**, *15*, 625–631. [CrossRef]
13. Eylon, D.; Froes, F.H. Titanium Net-Shape Technologies. *JOM* **1984**, *36*, 36–41. [CrossRef]
14. 46th ESAO Congress 3–7 September 2019 Hannover, Germany Abstracts. *Int. J. Artif. Organs* **2019**, *42*, 386–474. [CrossRef]
15. Garibov, G.S. Hot Isostatic Pressing of Ni Base Superalloy Discs Is a Main Development of New Mate rials for Production of Critical Gas Turbine Engine Components. In Proceedings of the International Conference on Hot Isostatic, Pressing, HIP'02, Moscow, Russia, 20–22 May 2002.
16. Ying, Z.; Sun, Y.; Zhang, X.; Wang, L.; Xu, G. Near-net Shaping of Titanium Alloy Powders by HIP Technology: A Review. *Mater. Rep.* **2019**, *33*, 1099–1108.
17. You, D.; Wang, Y.; Yang, C.; Li, F. Comparative analysis of the hot-isostatic-pressing densification behavior of atomized and milled Ti6Al4V powders. *J. Mater. Res. Technol.* **2020**, *9*, 3091–3108. [CrossRef]
18. Xu, G.; Zhang, X.; Zhao, C.; Wang, L.; Yin, Z. Microstructure of PM TC11 Alloy and Its Effect on Mechanical Behavior. *Aerosp. Mater. Technol.* **2013**, *43*, 110–113.
19. Procopio, A.T.; Zavaliangos, A. Simulation of multi-axial compaction of granular media from loose to high relative densities. *J. Mech. Phys. Solids* **2005**, *53*, 1523–1551. [CrossRef]
20. Yuan, W.X.; Mei, J.; Samarov, V.; Seliverstov, D.; Wu, X. Computer modelling and tooling design for near net shaped components using hot isostatic pressing. *J. Mater. Process. Tech.* **2006**, *182*, 39–49. [CrossRef]

21. Lu, H. Numerical Simulation and Experimental Study on the Near Net Forming of Inconel 625 Turbine Disk by Hot Isostatic Pressing. Master's Thesis, Huazhong University of Science and Technology, Wuhan, China, 2013.
22. Xu, W.; Lang, L.; Huang, X.; Li, F. Numerical simulation of complex thin-walled aluminum alloy part manufactured by hot isostatic pressing. *Forg. Stamp. Technol.* **2019**, *44*, 65–72.
23. Baccino, R.; Moret, F.; Pellerin, F.; Guichard, D.; Raisson, G. High performance and high complexity net shape parts for gas turbines: The ISOPREC (R) powder metallurgy process. *Mater. Des.* **2000**, *21*, 345–350. [CrossRef]
24. Chung, S.H.; Park, H.; Jeon, K.D.; Kim, K.T.; Hwang, S.M. An Optimal Container Design for Metal Powder under Hot Isostatic Pressing. *J. Eng. Mater. Technol.* **2001**, *123*, 234–244. [CrossRef]
25. Gang, W.; Lang, L.H.; Huang, X.N.; Liu, J.J. The shielding effect of capsule in the process of Hot Isostatic Pressing (HIP). In Proceedings of the 2016 13th International Bhurban Conference on Applied Sciences and Technology (IBCAST), Islamabad, Pakistan, 12–16 January 2016.
26. Zhou, S.; Song, B.; Xue, P.; Cai, C.; Liu, J.; Shi, Y. Numerical simulation and experimental investigation on densification, shape deformation, and stress distribution of Ti6Al4V compacts during hot isostatic pressing. *Int. J. Adv. Manuf. Technol.* **2017**, *88*, 19–31. [CrossRef]
27. Teraoku, T. Hot isostatic pressing simulation for titanium alloys. *Int. J. Powder Metall.* **2008**, *44*, 57–61.
28. Shima, S.; Oyane, M. Plasticity theory for porous metals. *Int. J. Mech. Sci.* **1976**, *18*, 285–291. [CrossRef]
29. Esaki, Y.; Matsushima, T.; Adachi, C. Current Enhancement in Organic Films through Gap Compression by Cold and Hot Isostatic Pressing. *Adv. Funct. Mater.* **2016**, *26*, 2940–2949. [CrossRef]
30. Gasik, M.; Zhang, B. A constitutive model and FE simulation for the sintering process of powder compacts. *Comput. Mater. Sci.* **2000**, *18*, 93–101. [CrossRef]
31. Ratchev, S.M.; Afazov, S.M.; Becker, A.A.; Liu, S. Mathematical modelling and integration of micro-scale residual stresses into axisymmetric FE models of Ti6Al4V alloy in turning. *Cirp J. Manuf. Sci. Technol.* **2011**, *4*, 80–89. [CrossRef]
32. Aryanpour, G. Constitutive Modeling for Hot Isostatic Pressing of Metal Powders. *J. Porous Media* **2006**, *9*, 15–34. [CrossRef]
33. Lee, D.N.; Kim, H.S. Plastic yield behavior of porous metals. *Powder Metall.* **1992**, *35*, 275–279. [CrossRef]
34. Fellah, M.; Hezil, N.; Samad, M.A.; Djellabi, R.; Montagne, A.; Mejias, A.; Kossman, S.; Iost, A.; Purnama, A.; Obrosov, A.; et al. Effect of Molybdenum Content on Structural, Mechanical, and Tribological Properties of Hot Isostatically Pressed β-Type Titanium Alloys for Orthopedic Applications. *J. Mater. Eng. Perform.* **2019**, *28*, 5988–5999. [CrossRef]
35. Ji, C.; Lang, L.; Huang, X.; Meng, F.; Xu, W. Study on the Powder Solid Interface and Coupled Deformation during high temperature and high pressure forming of Ti6Al4V Alloy Powder. *J. Cent. South Univ. (Sci. Technol.)* **2019**, *50*, 29–37.
36. Vattur Sundaram, M.; Khodaee, A.; Andersson, M.; Nyborg, L.; Melander, A. Experimental and finite element simulation study of capsule-free hot isostatic pressing of sintered gears. *Int. J. Adv. Manuf. Technol.* **2018**, *99*, 1725–1733. [CrossRef]

Disclaimer/Publisher's Note: The statements, opinions and data contained in all publications are solely those of the individual author(s) and contributor(s) and not of MDPI and/or the editor(s). MDPI and/or the editor(s) disclaim responsibility for any injury to people or property resulting from any ideas, methods, instructions or products referred to in the content.